

Stratified Turbulence and Mixing Efficiency in a Salt Wedge Estuary

R. C. HOLLEMAN,^a W. R. GEYER, AND D. K. RALSTON

*Department of Applied Ocean Physics and Engineering, Woods Hole Oceanographic Institution,
Woods Hole, Massachusetts*

(Manuscript received 10 October 2015, in final form 12 February 2016)

ABSTRACT

High-resolution observations of velocity, salinity, and turbulence quantities were collected in a salt wedge estuary to quantify the efficiency of stratified mixing in a high-energy environment. During the ebb tide, a mid-water column layer of strong shear and stratification developed, exhibiting near-critical gradient Richardson numbers and turbulent kinetic energy (TKE) dissipation rates greater than $10^{-4} \text{ m}^2 \text{ s}^{-3}$, based on inertial subrange spectra. Collocated estimates of scalar variance dissipation from microconductivity sensors were used to estimate buoyancy flux and the flux Richardson number Ri_f . The majority of the samples were outside the boundary layer, based on the ratio of Ozmidov and boundary length scales, and had a mean $Ri_f = 0.23 \pm 0.01$ (dissipation flux coefficient $\Gamma = 0.30 \pm 0.02$) and a median gradient Richardson number $Ri_g = 0.25$. The boundary-influenced subset of the data had decreased efficiency, with $Ri_f = 0.17 \pm 0.02$ ($\Gamma = 0.20 \pm 0.03$) and median $Ri_g = 0.16$. The relationship between Ri_f and Ri_g was consistent with a turbulent Prandtl number of 1. Acoustic backscatter imagery revealed coherent braids in the mixing layer during the early ebb and a transition to more homogeneous turbulence in the midebb. A temporal trend in efficiency was also visible, with higher efficiency in the early ebb and lower efficiency in the late ebb when the bottom boundary layer had greater influence on the flow. These findings show that mixing efficiency of turbulence in a continuously forced, energetic, free shear layer can be significantly greater than the broadly cited upper bound from Osborn of 0.15–0.17.

1. Introduction

The efficiency of stratified mixing is of great interest in oceanography and meteorology, as it determines the rate at which heat, salt, and passive scalars can be transported vertically in the ocean and atmosphere. The mixing efficiency, written as a flux Richardson number

$$Ri_f \equiv \frac{B}{P} \approx \frac{B}{B + \varepsilon}, \quad (1)$$

where B is buoyancy production, ε is turbulent kinetic energy (TKE) dissipation rate, and P is shear production, describes the apportioning of turbulent energy into buoyancy flux as opposed to TKE dissipation. In stably stratified flows, it is a measure of how efficiently

turbulence leads to the destruction of stable density gradients.

In addition to Ri_f , mixing efficiency is also often discussed in terms of the ratio $\Gamma \equiv B/\varepsilon$. Unlike Ri_f , Γ is not bounded by 0 and 1 and is more appropriately termed the dissipation flux coefficient (Moum 1996). To remain consistent with the notion of efficiency and better represent the connection with the gradient Richardson number, we will present efficiencies strictly as flux Richardson numbers, based on the approximation on the right-hand side of (1). Flux coefficient values from previous studies have been converted to equivalent flux Richardson numbers.

Estimates of mixing efficiency have been derived from theoretical, laboratory, numerical, and field studies. Osborn (1980) is one of the most cited studies, which suggested, based on previous theory and laboratory experiments, that $Ri_{f,\text{max}} = 0.15$, with 0.2 suggested as a practical upper bound for Γ (equivalent to $Ri_{f,\text{max}} = 0.17$). Oakey (1982) furnished the earliest estimate of Ri_f in a natural flow, finding $Ri_f = 0.19 \pm 0.09$. Seim and Gregg (1994), in a tidal channel with Kelvin–Helmholtz billows, found Ri_f to be between 0.08 and 0.39, with a nominal value of 0.22 [including the corrections from Seim and

^a Current affiliation: San Francisco Estuary Institute, Richmond, California.

Corresponding author address: R. C. Holleman, San Francisco Estuary Institute, 4911 Central Ave., Richmond, CA 94804.
E-mail: rustyh@sfei.org

Gregg (1995)]. Shaw et al. (2001) collected turbulence measurements in the continental shelf bottom boundary layer and found that mixing efficiency decreased to less than 0.05 in the lower 2 m of the water column. MacDonald and Geyer (2004), working in the energetic Fraser River, estimated buoyancy flux and turbulence production using an integral, control volume approach and found $Ri_f = 0.15$ to 0.2, along with TKE production rates as large as $10^{-3} \text{ m}^2 \text{ s}^{-3}$ and buoyancy Reynolds numbers (defined below) as high as 10^4 . Subsequent research has roughly supported the Osborn estimate; however, the uncertainty of field estimates is large, with Ri_f ranging from 0.05 to 0.29 (summarized in Ruddick et al. 1997; Thorpe 2005; Inoue and Smyth 2009).

In field observations, the most common approach to quantifying mixing efficiency is with microstructure measurements that resolve the dissipation range for both temperature and shear. Microstructure profiles typically do not resolve the entire dissipation range, and rely instead on a universal spectrum to account for the unresolved portion, a step that can be tedious and ill posed when measuring high dissipation rates, particularly when using temperature probes (Gregg 1999). Dissipation range measurements are typically made in open water where dissipation rates are relatively weak (up to $10^{-6} \text{ m}^2 \text{ s}^{-3}$) and depths are sufficient to allow for profilers to reach terminal velocity. Applying these methods in energetic, shallow flows is difficult as water depths are insufficient for free-falling profilers to reach a steady velocity, the limited spatial response of the probes cannot resolve finescale structure (Macoun and Lueck 2004), and fast sample rates are susceptible to noise (Peters 1997). Furthermore, the dominance of salt stratification over temperature in estuarine flows requires resolving a scalar variance dissipation range at wavenumbers greater than for temperature alone because of the difference between the Prandtl number (approximately 7) and Schmidt number (approximately 700 for salt).

In sufficiently energetic flows, ε and χ_s (dissipation rate of turbulent salinity variance) can be measured from the inertial subrange of the power spectrum (Shaw et al. 2001). Measurements in the inertial subrange have lower requirements for sample rate, permitting the use of acoustic Doppler velocimeters (ADVs) for velocity variance. While the dissipation range for salinity variance is difficult to measure, the inertial-convective and viscous-convective subranges are broad and resolvable by microconductivity cells (Lavery et al. 2013). Inertial subrange measurements have been successfully applied to data from ship-mounted ADVs (Scully et al. 2011; Lavery et al. 2013), a situation where vibration would complicate the use of dissipation range measurements with shear probes.

An alternative approach to understanding mixing efficiency is to simulate turbulent mixing with direct numeric simulation (DNS), and several such experiments with shear instabilities have found higher efficiencies than the canonical Osborn value. Smyth et al. (2001) estimated efficiency as a function of time, finding asymptotic values of 0.23–0.29 for a Prandtl number of $Pr = 1$ and 0.17 for cases with Pr between 2 and 7. Their suggested model $\Gamma = 0.33 \hat{R}_{OT}^{-0.63}$ (where \hat{R}_{OT} is a measure of the age of the mixing event, defined as the ratio of the Ozmidov scale to the Thorpe scale) suggests that continually forced turbulence would have $Ri_f = 0.25$. Mashayek and Peltier (2013) concluded that $Ri_f = 1/3$ in DNS experiments of shear instability at Reynolds numbers up to 10^4 , citing the role of intermediate-scale stirring motions as an explanation for the high efficiency.

An important differentiator among turbulence studies is the role of intermittency and unsteady forcing. Studies such as Smyth et al. (2001), Inoue and Smyth (2009), and Mashayek and Peltier (2013) focused on the evolution of an isolated or transiently forced turbulent event and the corresponding evolution of the mixing efficiency. These experiments may include a highly efficient, preturbulent phase in which diffusion is enhanced by two-dimensional, nonturbulent straining of the scalar field and a decay phase in which the efficiency decreases as the turbulence “ages.” While qualitative differences between simulated and observed shear instabilities persist, DNS findings suggest that the mixing efficiency has an upper bound greater than the value of 0.17 from Osborn (1980), particularly before the decay phase of a turbulent patch.

The buoyancy Reynolds number, also called the activity number or Gibson number, is defined as $Re_b \equiv \varepsilon/\nu N^2$, where ν is molecular viscosity and $N^2 \equiv -(g/\rho)\partial\rho/\partial z$ is the buoyancy frequency. It is often used to describe the state of stratified turbulence and the degree to which it is affected by stratification and viscosity (Gibson 1986; Ivey and Imberger 1991; Stacey et al. 1999). Laboratory experiments have found that turbulence is suppressed for $Re_b \leq 15$ (Saggio and Imberger 2001). Dependence of the mixing efficiency on Re_b was investigated experimentally by Barry et al. (2001) and numerically by Shih et al. (2005), both of whom found that the maximum efficiency was similar to the $Ri_f \approx 0.17$ of Osborn (1980) and was a decreasing function of Re_b for $Re_b > 100$. This is in contrast to field studies in highly stratified estuaries that have found $Ri_f \approx 0.18$ to 0.26 with $Re_b \approx 10^4$ – 10^5 (Kay and Jay 2003) and $Ri_f \approx 0.15$ at Re_b on the order of 10^4 (MacDonald and Geyer 2004).

Salt wedge estuaries provide high-energy shear flows suitable for the study of stratified mixing at large values

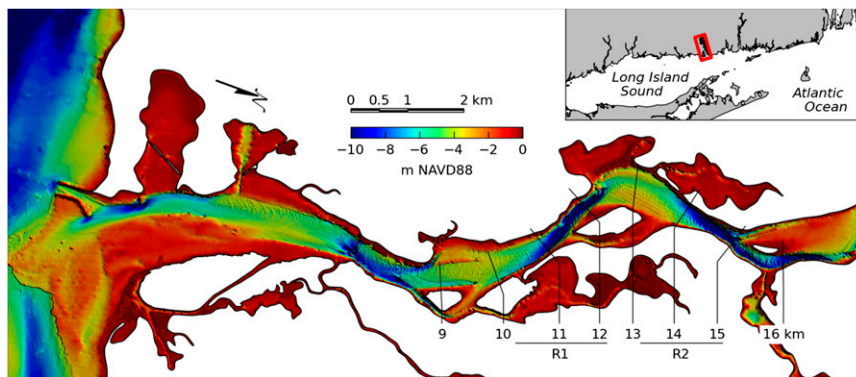


FIG. 1. Connecticut River estuary bathymetry, with river kilometer and the two study sites labeled. The red rectangle in the inset denotes location relative to Long Island Sound.

of Re_b (Geyer et al. 2008). A continuous source of buoyancy is supplied by the density contrast between the river outflow and the ocean, and energy for turbulence is provided by the tidal flow. The energy levels in these environments are large enough that there is a well-developed inertial subrange in velocity variance, allowing ε to be determined from the height of the spectrum of turbulence-resolving vertical velocity time series within the stratified shear layer (Kaimal et al. 1972; Scully et al. 2011). While some details of the geometry and forcing of these flows are specific to salt wedge estuaries, many aspects of the mixing are relevant to other shear flows with persistent forcing or the presence of boundaries. More broadly, stratified mixing at a high Reynolds number is relevant in a wide range of estuarine and oceanic flows (Mashayek and Peltier 2013).

In addition to inertial subrange methods, acoustic backscatter is also well suited to visualizing and quantifying turbulent mixing in conditions typical of salt wedge estuaries (Lavery et al. 2013). Backscatter is sensitive primarily to microstructure in the viscous-convective subrange. In salt-dominated stratified turbulence, the height of the salinity variance spectrum can be derived from the backscatter intensity and is indicative of enhanced scalar variance dissipation. While backscatter alone does not permit an estimate of the mixing efficiency, it does reveal the spatial structure of mixing intensity. For example, measurements in the salt wedge of the Connecticut River revealed large-amplitude shear instabilities, marked by intensified mixing along the braids of the instabilities (Lavery et al. 2013).

We collected stratified turbulence measurements in the Connecticut River, utilizing in situ inertial subrange methods suitable for energetic tidal flows. The measurements included both TKE dissipation rates and scalar variance dissipation rates, supporting the calculation of flux Richardson numbers. These measurements characterized mixing processes at significantly greater

bulk Reynolds number and buoyancy Reynolds number than are currently feasible in laboratory or DNS experiments.

2. Methods

Shipboard measurements were collected in the Connecticut River estuary (Fig. 1) from 4 to 8 November 2013 during a period of spring tides and moderate river discharge of $200\text{--}400\text{ m}^3\text{ s}^{-1}$. The measurements and analysis focused on observations within two reaches defined by channel constrictions, referred to here as frontal zones due to the formation of bottom-trapped salinity fronts during the ebb tide. The reaches were located 11 (R1) and 14 km (R2) from the river mouth.

Surveys were conducted from the 60 ft R/V *Tioga*. Mean current measurements were collected using a ship-mounted 1200-kHz RDI acoustic Doppler current profiler (ADCP). Collocated with the ADCP was a suite of EdgeTech broadband acoustic transducers, of which the 450–590-kHz channel was used in this study. The Mobile Array for Sensing Turbulence (MAST; Geyer et al. 2008) was deployed from the R/V *Tioga* as shown in Fig. 2. The MAST comprises a series of eight instrument clusters mounted onto a 10-m spar, pivoting from a point off the starboard bow, outboard of the ship's wake. When sampling in water shallower than the maximum depth of the MAST (approximately 40% of the time), it was raised just enough to clear the bed, using an altimeter to monitor the clearance. Data contaminated by vibrations due to grazing the bed or raising and lowering the MAST were removed from the analysis. Each cluster included an RBR conductivity-temperature-depth (CTD) sensor sampling at 6 Hz, a Sontek acoustic Doppler velocimeter sampling at 25 Hz, and a Sea-Bird Electronics SBE-7 microconductivity sensor sampling at 300 Hz. CTD data revealed a linear relationship between temperature T and salinity s with a

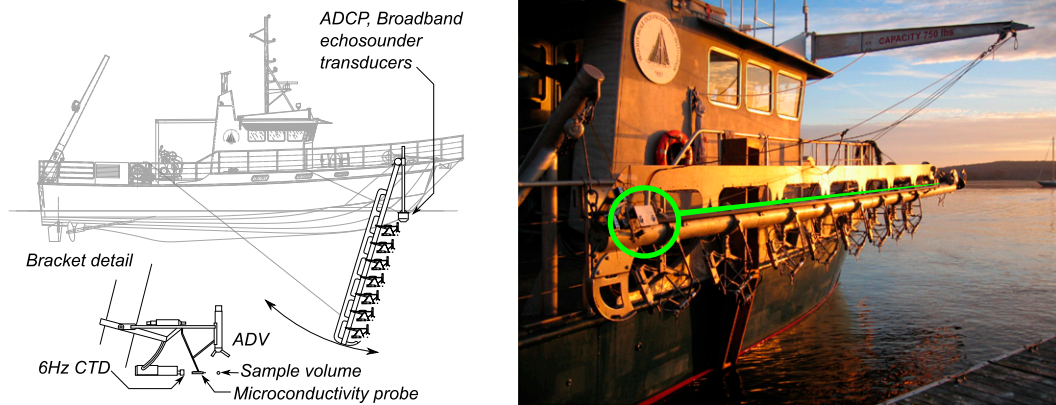


FIG. 2. (left) Schematic of MAST and profiler and (right) R/V *Tioga* in the Connecticut River; green highlights show trolley mount and track.

slope $\Delta T/\Delta s = 0.074$, indicating that variations in density and conductivity were dominated by salinity. Turbulent fluctuations were sufficiently characterized by microconductivity, without needing to resolve temperature microstructure or contend with the challenges of sensor response mismatch and differing Batchelor scales for temperature and salinity (Nash and Moum 2002). In addition to the fixed sensor clusters, a motorized trolley ran along the lower 8 m of the MAST, carrying an RBR CTD and SBE-7 microconductivity sensor. During most transects, the trolley was run continuously, repeating an up-down cycle every 15 s. A separate profiling CTD was deployed in a tow-yoing configuration from the port side, with a protective cage that allowed for it to graze the bed on each cast without damaging the conductivity probe. While the trolley profiler sampled only the upper 7 m of the water column due to the length of the spar, the tow-yoing profiler sampled to within about 0.35 m of the bed. Transects were approximately parallel to the thalweg, with the ship following the direction of the surface currents. Each transect took approximately 15 min.

Turbulence data were calculated from time series of ADV velocity and SBE microconductivity, processed in 20-s windows with 50% overlap between successive windows (e.g., Figs. 3a,c). Power spectra of vertical velocity were used to find ε by fitting the form

$$S_{ww}(k) = a_0 \varepsilon^{2/3} k^{-5/3}, \quad (2)$$

in which S_{ww} is the power spectral density of vertical velocity fluctuations, $a_0 = 0.68$ is the Kolmogorov constant, and k is the wavenumber (Tennekes and Lumley 1972; Shaw et al. 2001; Geyer et al. 2008).

An essential aspect of this method is determination of the existence and bounds of the inertial subrange. The minimum wavenumber of the inertial subrange is set by the reciprocal of the Ozmidov length scale

$$L_o \equiv \left(\frac{\varepsilon}{N^3} \right)^{1/2}. \quad (3)$$

The observable inertial subrange is further limited by ship motion and surface gravity wave contamination at frequencies below 1 Hz. The maximum wavenumber of the inertial subrange is determined by molecular viscosity and the TKE dissipation rate via the Kolmogorov scale. At the high-wavenumber end, the observable subrange is also limited by the Nyquist cutoff of the ADVs and the noise floor of the instrument. The upper- and lower-wavenumber bounds of the inertial subrange were based initially on an assumed maximum value of $10^{-3} \text{ m}^2 \text{ s}^{-3}$ for the TKE dissipation rate and were then iteratively updated based on successive estimates of dissipation rate. The height of the inertial subrange (i.e., the nominal value of $S_{ww}/k^{-5/3}$) was taken from the 1.6-octave interval with a slope closest to $-5/3$ in order to further avoid contamination from waves and noise. Samples for which the best slope was outside the range $[-7/3, -1]$ were discarded. The spectral height can then be directly related to the TKE dissipation rate with (2). An illustration of the spectral fit and constraints on the inertial subrange is shown in Fig. 3b.

Similarly, scalar variance dissipation rates can be estimated with the turbulence-resolving time series of salinity, which dominates density variations in estuarine environments. With sufficiently fast sampling rates, not only can the inertial subrange be resolved but a portion of the viscous-convective subrange can also be resolved, with a combined spectral shape

$$S_{ss}(k) = b_0 \chi_s \varepsilon^{-1/3} k^{-1} \min(k, k_\eta)^{-2/3}, \quad (4)$$

where χ_s is the dissipation rate of turbulent salinity variance, S_{ss} is the power spectral density of salinity variance, and $b_0 = 0.40$ is the Kolmogorov constant for

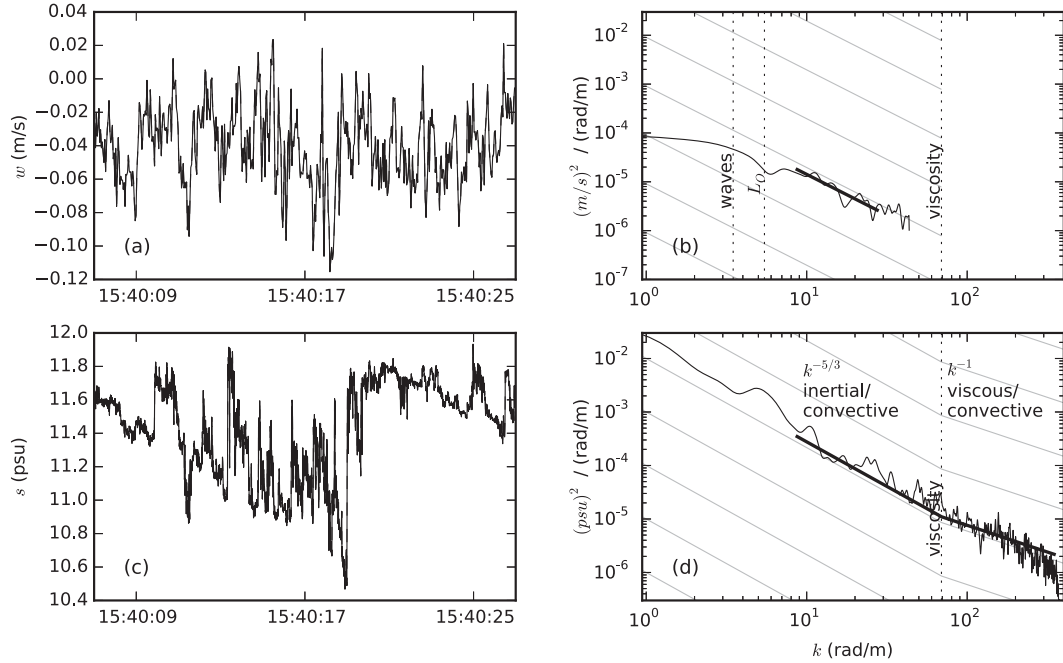


FIG. 3. (a) The w' time series over a typical 20-s interval, (b) inertial subrange analysis of w' , (c) fast conductivity time series (converted to salinity), and (d) fast conductivity inertial/viscous-convective subrange analysis.

scalar variance. The wavenumber $k_\eta = 0.04(\epsilon/\nu^3)^{1/4}$, with ϵ supplied by the ADV analysis, is proportional to the Kolmogorov wavenumber and describes the inertial-viscous transition where the spectral slope transitions from an inertial-convective $k^{-5/3}$ spectrum to a k^{-1} viscous-convective spectrum (Lavery et al. 2013). The spectral shape in (4) was fit to the observed spectrum across wavenumbers ranging from the lower-bound wavenumber used in the ADV spectral fit up to the wavenumber corresponding to the 100-Hz antialiasing filter of the conductivity sensor (Fig. 3d).

Buoyancy flux was estimated from χ_s and $\partial s/\partial z$ by assuming that scalar variance production and dissipation were in balance:

$$\overline{s'w'} \frac{\partial s}{\partial z} \approx \frac{\chi_s}{2}, \quad (5)$$

leading to

$$B \approx -\frac{g\beta\chi_s}{2\frac{\partial s}{\partial z}} \quad (6)$$

(Osborn and Cox 1972). The buoyancy flux was combined with the TKE dissipation rate from (2) to calculate a mixing efficiency via (1). Ruddick et al. (1997) termed the efficiency deduced from this method an apparent mixing efficiency (specifically in reference to the corresponding flux coefficient), as its equivalence

to the true mixing efficiency requires that (i) mean quantities are averaged over spatial scales larger than the turbulent length scale, (ii) turbulence is in quasi equilibrium, and (iii) the Reynolds number is sufficiently large to assume that eddy diffusivities of salt and density are the same. The first and third criteria are easily met in the present data. The second criterion could potentially be compromised by time dependence, advection, or turbulent transport of TKE. Given the persistence and spatial scales of the mixing regions, neither time dependence nor advection was likely a significant contributor to the TKE balance at scales significantly larger than the individual instability events. Vertical TKE transport was more difficult to rule out, but as discussed further in section 4 the expected effect on estimated efficiencies is minimal.

Stratification has a deceptively simple definition in N^2 , but in practice it is difficult to calculate at the dynamically appropriate scales, and N^2 can introduce scatter and bias into the mixing efficiency results because of its appearance in the denominator of (6). Methods for calculating a dynamically relevant stratification in the ocean have been explored by Smyth et al. (2001) as well as others, though these methods assume the microstructure measurements were collected from a profiling platform and leverage collocated overturn, dissipation, and stratification data. In the present study, microstructure measurements from a constant elevation instrument cluster on the MAST were related to separate, temporally sparser profiles of stratification. To calculate

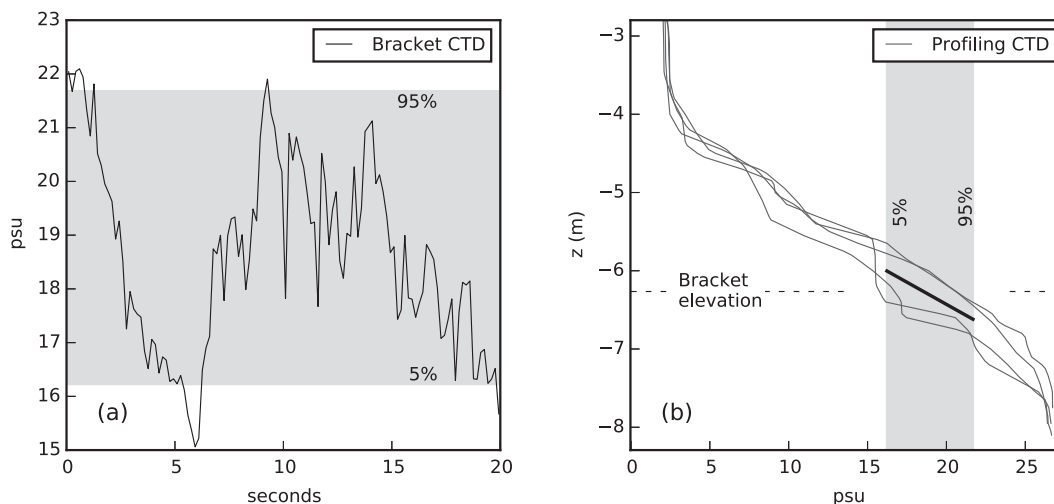


FIG. 4. Illustration of method for calculating $\partial s/\partial z$. (a) Time series of salinity from MAST-mounted CTD and (b) vertical profiles of salinity within 30 s of the period in (a), where shading indicates the set of samples used in calculating $\partial s/\partial z$ and the heavy line indicates the fit.

stratification, we utilized a method, illustrated in Fig. 4, that linked the constant elevation time series of salinity with the vertical profiles. For each 20-s window over which turbulence parameters were to be estimated, the relevant salinity range was defined as the 5th–95th percentile range of salinity from the CTD on the MAST. For each CTD profile within 30 s of the turbulence time window, the salinity was stably sorted, and those samples falling within the 5th–95th percentile range were extracted along with their vertical coordinates. A line was fit to this population of salinity/elevation samples, and the mean slope across the profiles gave a representative $\partial s/\partial z$. Using the variation of salinity at a constant elevation in conjunction with a vertical profile is similar to using the Ellison scale (Ellison 1957),

$$L_E \equiv \frac{(\overline{\rho'^2})^{1/2}}{\frac{\partial \rho}{\partial z}}, \quad (7)$$

for characterizing turbulence length scales based on the time variation of water properties. However, here we are not assuming that the fluctuations are due to turbulence but may also be due to coherent disturbances in the pycnocline. For example, the salinity range in Fig. 4 implied a vertical averaging scale of $(s_5 - s_{95})/(\partial s/\partial z) = 0.62$ m (where s_i is the i th percentile salinity value). In contrast, the Thorpe scale (Thorpe 1977; Dillon 1982), for the profile centered on the time period shown in the figure, was 0.08 m. This suggests that salinity variations observed by the constant elevation CTDs were affected by larger motions and not just individual overturns. The newly developed method provides a rational and robust

means of selecting the vertical scale for estimating N^2 . Unlike methods defined relative to discrete overturning patches (where a small perturbation in the density profile may result in a large difference in patch boundaries), the present method also yields a N^2 that is a continuous function of the observations. The following section includes a comparison between this approach and three other methods for estimating N .

3. Results

The analysis focused on conditions during the ebb in frontal zones R1 and R2. The ebb flow in the frontal zones was nearly steady and uniform in the along-channel direction, with a gradual deepening of the pycnocline through the course of the ebb. This led to a mean salinity field that was relatively stationary across successive casts, and multiple repeats of the same transect captured a smooth transition between early ebb and late ebb states. While data were also collected during flood tides, the flow during the flood was more unsteady because of the landward advection of the salt wedge. Given the difficulties in extracting robust gradients and turbulence data from these unsteady, irregular conditions, the analysis was limited to ebb conditions.

a. Mean flow

The mean flow typically exhibited a layer of intense shear and stratification in the early ebb, such as in the transect shown in Fig. 5a. Gradients in velocity and salinity were concentrated in a mixing layer roughly 3 m thick and centered about 3 m above the bed, with lower-layer velocities slightly landward and upper-layer

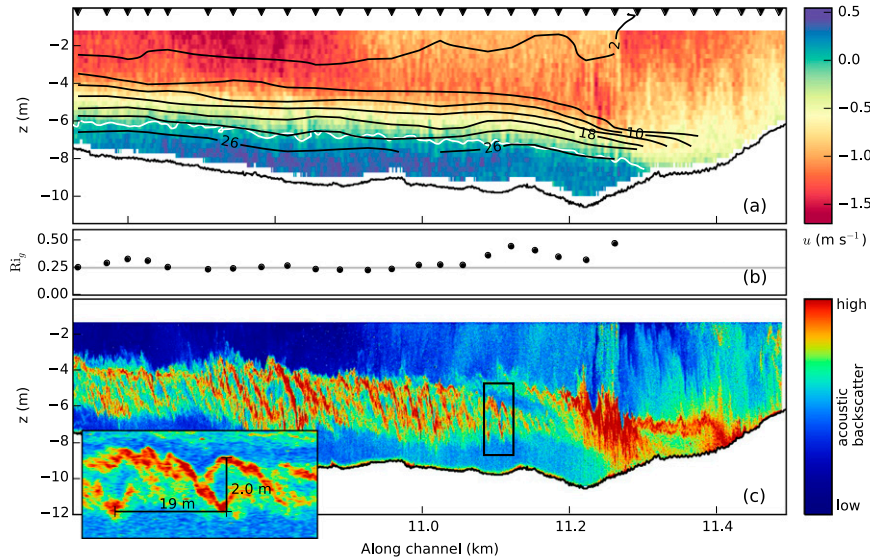


FIG. 5. Transects in R1 [1425 eastern standard time (EST) 4 Nov 2013]. Seaward is to the left. (a) Along-channel velocity pseudocolor; positive is flood directed. Isohalines from the tow-yoing CTD profiler are plotted every 4 psu; black triangles indicate individual casts. Velocity and salinity data have been low-pass filtered at 0.75 m in the vertical and 50 m in the horizontal. A reduction in the surface velocity at 11–11.2 km is due to a side channel. (b) Pycnocline Ri_g . (c) Broadband acoustic backscatter over 450–590 kHz. The inset shows a detail of an instability with the distance between core regions and height of the instability annotated.

velocities reaching 1.5 m s^{-1} seaward. The distribution of the gradient Richardson number $Ri_g \equiv N^2/(\partial u/\partial z)^2$ along the transect is shown in Fig. 5b, where Ri_g has been calculated as an average over the pycnocline (defined as 6–24 psu). The Ri_g remained near the critical value of $1/4$ through most of the transect, with the exception of transient adjustments near the toe of the salt wedge. Acoustic backscatter along this transect (Fig. 5c) showed large-scale coherent braid structures in the mixing layer, indicative of shear instabilities with wavelengths on the order of 20 m (see inset). Salinity variability associated with these instabilities is not visible in Fig. 5a as their wavelengths were not resolved in the interpolated salinity field. Increased backscatter was evident in the instabilities, indicating enhanced dissipation of salinity variance (Lavery et al. 2013). The slanting, linear organization of the intensified backscatter is consistent with strong turbulent production and mixing along highly strained braids, with relatively little mixing in the intervening “core” regions. Coherent braid structures were common in early and midebb transects that had a midwater column shear layer, with the braid–core organization typically most distinct at the upstream end of each transect. Lumps along the braids, for example, the upper-left portion of the inset in Fig. 5c, were likely secondary instabilities.

b. Vertical microstructure

Representative vertical microstructure profiles, taken from this same transect at 10.8 km, are shown in Fig. 6. Significant variation is apparent between the multiple microstructure casts (plotted in gray), as the profiler sampled varying portions of the coherent structures visible in the acoustics. While the vertical extent of the instabilities reached nearly 3 m, visible in the backscatter, the vertical overturn scale was much smaller. The mean Thorpe scale calculated from the profiles shown in Fig. 6, at an elevation of -5 m , was 0.21 m, and Ozmidov scales (discussed below) had a mean of 0.24 m in the same vicinity. The profile of the gradient Richardson number (calculated over vertical scales of 1.5 m) is near the critical value of $1/4$ within most of the pycnocline. The bulk Reynolds number for a free shear layer

$$Re \equiv \frac{\frac{1}{2}\Delta U \frac{1}{2}\Delta z}{\nu} \quad (8)$$

(as Re typically is estimated for shear layers; e.g., Smyth et al. 2001; Mashayek et al. 2013) is approximately 5×10^5 for the profile shown in Fig. 6. As the ebb progressed, the salt wedge eroded and the elevation of the mixing layer decreased. Near the middle of the ebb the flow transitioned to a stratified bottom boundary layer, in which the

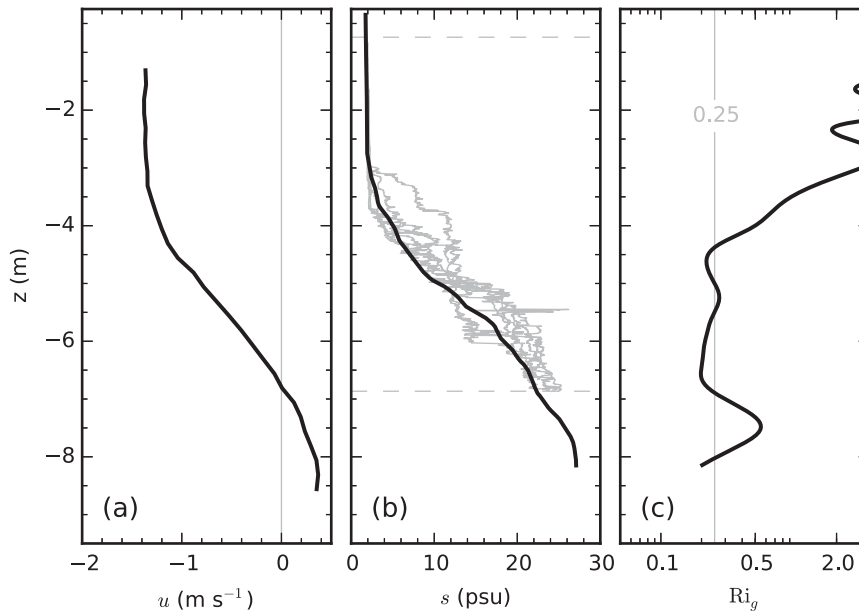


FIG. 6. Vertical profiles near 10.8 km (1425 EST 4 Nov 2013) of (a) along-channel velocity averaged over 100 s, (b) salinity from tow-yo CTD (black) and trolley-mounted micro-conductivity (gray), and (c) Ri_g , averaged over 1.5 m (log scaled).

maximum shear was located at the bed, and the acoustics no longer showed coherent mixing structures. During these field observations both R1 and R2 were completely fresh by the end of ebb.

c. Turbulence quantities

Estimates of ε , χ_s , and B were calculated for 26 transects during the ebb tide. An example of the spatial distributions of ε and χ_s during the early ebb is shown in Fig. 7, overlaid on acoustic backscatter imagery. In a significant number of samples the inertial range was not resolved by the measurements. The most common cause for an unresolvable inertial subrange was small dissipation rates that effectively shifted the spectrum below the ADV noise floor. Other causes included periods when the MAST was being raised or lowered, surface wave contamination, and a few cases when strong stratification shifted the inertial subrange beyond the Nyquist cutoff. All of the following analyses were limited to samples for which $N\partial u/\partial z > 0.01 \text{ s}^{-2}$, corresponding to 21% of the samples. This criterion restricts the analyses to portions of the domain with significant mixing, omitting unstratified and low-energy regions outside the primary mixing layer. The inertial subrange was resolvable in 47% of the samples satisfying this threshold.

The braids visible in the acoustic backscatter were not resolved by the 20-s averaging period of the spectral quantities (corresponding to approximately 30-m spatial averages). However, the spectral estimates are correlated

with acoustic backscatter intensity at larger scales, such as the intensification of mixing at 10.8 km (Fig. 7). The largest dissipation rates were consistently within the pycnocline, and in this region ε and χ_s are highly correlated. Outside the pycnocline ε decreased by an order of magnitude, while χ_s decreased by two orders of magnitude, as both the turbulence intensity and the ambient salinity gradient were weaker.

A transect from the late ebb is shown in Fig. 8. By this point in the tide the upper-water column was unstratified and fresh. A stratified bottom boundary layer existed seaward of 11.0 km, visible in Fig. 8 as a 3-m-thick layer adjacent to the bed in which χ_s is nonnegligible and ε decreases with distance from the bed. The portion of R1 included in this transect had large, distinct bedforms, likely contributing to greater boundary layer mixing compared to transects where the sandy bottom had no bedforms. The acoustic backscatter in the lowest 3 m was also greater than backscatter higher in the water column, though it is difficult here to disentangle the effects of backscatter due to suspended sediment and stratified mixing. While portions of the unstratified water had large dissipation rates, χ_s was small due to the weak $\partial s/\partial z$ in these areas and was often undetectable outside the stratified bottom boundary layer.

d. Mixing efficiency

Mixing efficiency, represented by Ri_f , was calculated from ε and B via the right-hand side of (1). Each

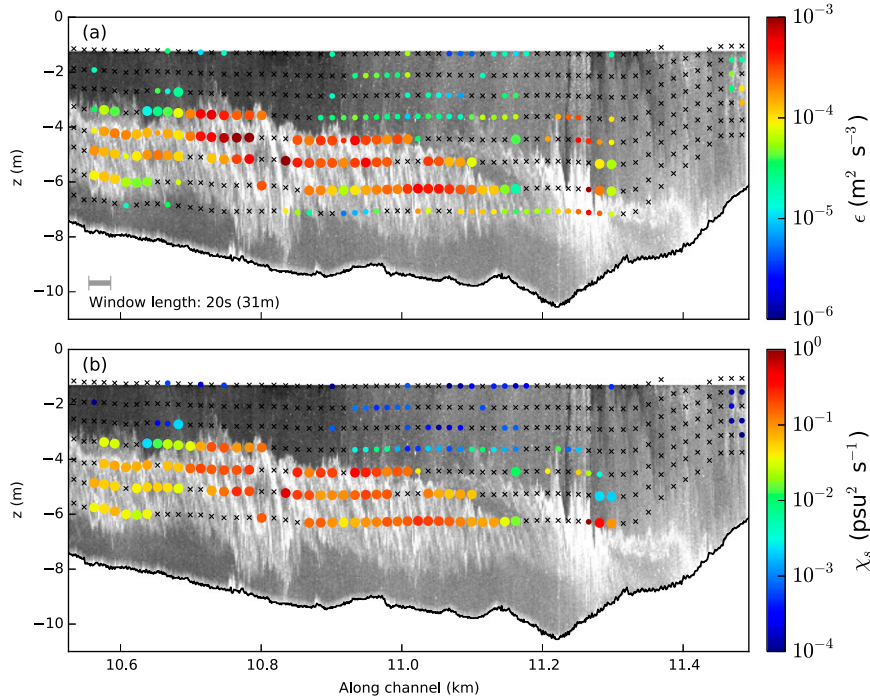


FIG. 7. Spatial distribution of (a) ϵ and (b) χ_s in the stratified shear layer of the early ebb (1425 EST 4 Nov 2013), overlaid on acoustic backscatter imagery. Small dots signify samples for which $N\partial u/\partial z < 0.01 \text{ s}^{-2}$ and are not included in later statistics, and \times marks samples for which the inertial range was not adequately resolved.

estimate of Ri_f was calculated from collocated estimates of ϵ , χ_s , and a representative $\partial s/\partial z$ calculated as illustrated in Fig. 4. Individual estimates of Ri_f have a spatial resolution of approximately 30 m in the horizontal and 1 m in the vertical but were highly variable due to the stochastic nature of turbulence quantities and the heterogeneous flow conditions. To obtain a more aggregated view, distributions of Ri_f were calculated for 19 transects in R1 and R2, spanning the majority of the ebb tide (several transects did not contain enough data points to support per transect statistics). Figure 9 shows mean efficiency as a function of the tidal phase. The tidal phase is expressed as the time since the beginning of the ebb based on depth-averaged velocities from a moored ADCP in R1 at 11.2 km. The per transect mean efficiencies fall within the range 0.15–0.27. A trend is visible with mean efficiency declining over the course of the tide, such that efficiency before hour 3 is centered around 0.23, and after hour 3 the mean Ri_f is approximately 0.17. The first 2.5 h of the ebb showed significant variation in efficiency, reflecting the greater temporal and spatial variability of the mean structure during this period. In particular, early ebb transects in R1 with small mean Ri_f tended to have highly stratified, thin pycnoclines

without significant mixing, with mean Ri_f dominated by measurements below the pycnocline.

One possible explanation for the variation in efficiency between transects is the variability in how much the boundary contributes to shear production and constrains the length scales of turbulent motions. We focused on the effects of the bottom boundary and, similar to the scaling in Scully et al. (2011), compared the Ozmidov scale

$$L_o = \left(\frac{\epsilon}{N^3}\right)^{1/2} \tag{9}$$

to the log-layer length scale κz via the ratio $L_o/\kappa z$, where $\kappa = 0.4$ is the von Kármán constant, and z is the distance from the bed. Figure 10 shows the population of Ri_f estimates, categorized relative to a threshold value of $L_o/\kappa z = 0.25$. This threshold was chosen based on the results of Scully et al. (2011), the observed rolloff in the efficiencies around this value, and the need to have a statistically meaningful number of samples in the boundary-influenced $L_o/\kappa z > 0.25$ category. Ozmidov-limited samples ($L_o/\kappa z < 0.25$) made up 86% of the data. The mean efficiency for the Ozmidov-limited samples, calculated over log-spaced windows (5 decade^{-1}), ranged from 0.20 to 0.24, with a slight decreasing trend as Re_b increased

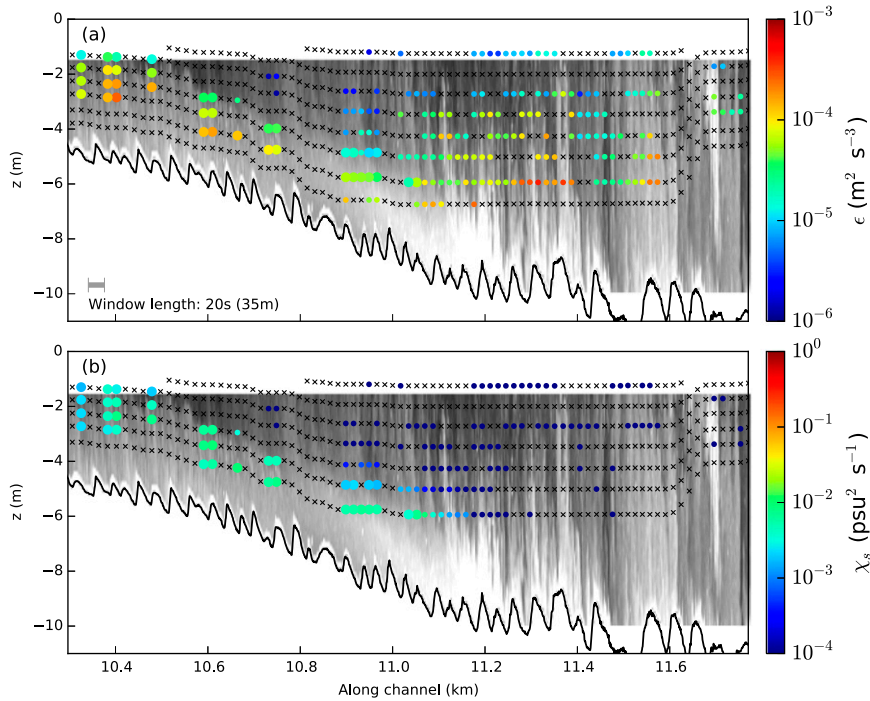


FIG. 8. As in Fig. 7, but for the stratified boundary layer of the late ebb (1715 EST 5 Nov 2013).

from 400 to 10 000. The mean efficiency over all of the Ozmidov-limited samples was 0.23 ± 0.01 (where the 95% confidence interval was calculated via bootstrapping), with a per sample standard deviation of 0.09. Boundary-influenced samples had significantly lower mixing efficiency (0.17 ± 0.02) and a more pronounced rolloff at large Re_b . Gradient Richardson numbers for the Ozmidov-limited and boundary-influenced populations are summarized in Fig. 10b, showing the median and interquartile range. Median Ri_g was 0.25 for Ozmidov-limited samples and 0.16 for boundary-influenced samples.

While the dominant feature in Fig. 10 is the difference in mean efficiency between the two categories, more subtle trends are also evident. Efficiency among the Ozmidov-limited samples is weakly anticorrelated with Re_b , though the trend is not significantly greater than the width of the confidence intervals. Apparent trends in Ri_f as a function of Re_b may be biased by variance in the observed quantities, particularly statistical turbulence descriptors with broad natural variance such as ϵ and the salinity power spectrum. The essential observed parameters were ϵ , H_{ss} (height of the salinity variance power spectrum), and $\partial s/\partial z$. Of these quantities, ϵ and $\partial s/\partial z$ appear in both Ri_f and Re_b , such that variance in the observations could contribute to artificial trends in the correlation between Ri_f and Re_b . With ϵ appearing in the denominator of Ri_f and the numerator of Re_b , variance in ϵ uncorrelated with the other quantities would create an apparent negative

correlation between Ri_f and Re_b . To quantify this effect, we generated synthetic datasets based on the observed values of H_{ss} and $\partial s/\partial z$ and a synthetic $\hat{\epsilon}$:

$$\hat{\epsilon} = X \left(\frac{gBH_{ss}}{2b_0 \frac{\partial s}{\partial z}} \frac{1 - R_{f,0}}{R_{f,0}} \right)^{3/2}, \quad (10)$$

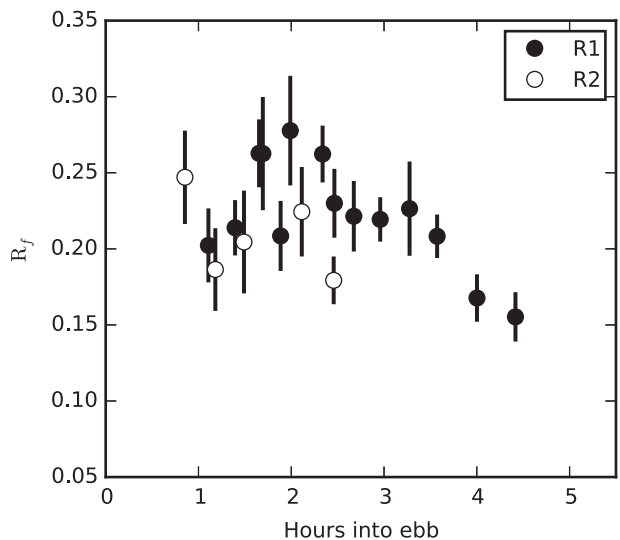


FIG. 9. Mean Ri_f and two standard error intervals, aggregated by transect. Start of ebb is derived from depth-averaged currents in R1.

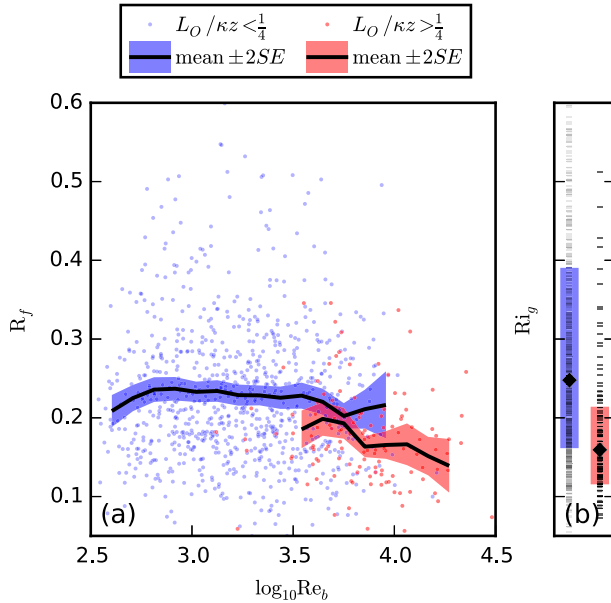


FIG. 10. (a) Behavior of Ri_f as a function of Re_b . Samples and means are colored by whether the turbulent overturns are Ozmidov-limited (blue) or boundary-influenced (red). (b) Median and interquartile range of Ri_g for the same categories of Ozmidov-limited and boundary-influenced. Individual samples are shown as gray ticks. The vertical axis is cropped and omits 1% of Ri_f values and 9% of Ri_g values.

where Ri_{f0} is the “true” efficiency of the synthetic data, and X is a log normally distributed random variable with mean of 1. The slope and intercept of the Ozmidov-limited samples in Fig. 10 were reproduced in the synthetic dataset with $Ri_{f0} = 0.22$ and X having a standard deviation of 0.33 (equivalent to the root-mean-square relative error in ε). While a 33% relative error may sound large, we note that ε is the result of a fit in log–log space and that the variance of Ri_f in the synthetic dataset is still less than half of the variance in the observations. In contrast to ε , $\partial s/\partial z$ appears in the denominators of Ri_f and Re_b , and uncorrelated variance in $\partial s/\partial z$ would lead to an apparent positive correlation between Ri_f and Re_b . The synthetic data analysis demonstrates that the observations are entirely consistent with an asymptotic efficiency for Ozmidov-limited samples, that is, that at sufficiently high Re_b and Re , $Ri_{f,max}$ is independent of Re and Re_b . It also shows that compensating for the minor trend does not significantly alter the estimated mean efficiency.

e. Stratification estimates

A central source of uncertainty in B comes from the estimate of stratification N because of the difficulty in identifying the density gradients, past and present, against which the turbulence has acted. The above results are based on estimates of N utilizing the method

TABLE 1. Comparison of stratification estimates.

Method	Correlation with N_{ref}	Regression against N_{ref}	Ozmidov-limited Ri_f
N_{ref}	—	—	0.227 ± 0.008
$N_{1.0}$	0.88	$0.92N_{ref} + 0.01$	0.241 ± 0.010
$N_{0.1}$	0.77	$0.93N_{ref} + 0.00$	0.278 ± 0.012
N_b	0.85	$0.81N_{ref} + 0.03$	0.218 ± 0.007

described in section 2. Comparisons were made between that method (denoted here as N_{ref}) and three other estimates of N to assess the robustness of the results. The other methods are (i) a simple finite difference across brackets of the MAST (N_b), (ii) 1.0-m vertical averages of $\partial s/\partial z$ from CTD profiles overlapping the analysis window ($N_{1.0}$), and (iii) 0.1-m vertical averages of $\partial s/\partial z$ from CTD profiles overlapping the analysis window ($N_{0.1}$). The comparison is summarized in Table 1. Mixing efficiency was estimated for the Ozmidov-limited samples using each of the stratification estimates. The Ozmidov-limited subset was chosen for this test since it is the most likely to have a constant efficiency. Results were similar across N_{ref} , $N_{1.0}$, and N_b , while $N_{0.1}$ yielded significantly higher efficiencies. The width of the 95% confidence interval on Ri_f was practically the same in all cases. Comparisons across the boundary-influenced samples were similar. Overall, results were clustered around N_{ref} and essentially indistinguishable between N_{ref} , $N_{1.0}$, and N_b , with $N_{0.1}$ as a distinct outlier.

4. Discussion

The mean mixing efficiency in Ozmidov-limited samples was found to be $Ri_f = 0.23 \pm 0.01$, with a standard deviation for individual samples of 0.09. Mean efficiency decreased to 0.17 ± 0.02 for the subset of samples in which mixing was likely influenced by the boundary. The nominal mixing efficiency of the Ozmidov-limited samples is significantly greater than the maximum of 0.17 described in Osborn (1980), a value often assumed when mixing efficiency cannot be estimated (e.g., Müller and Garrett 2002; St. Laurent et al. 2001; Moum et al. 2003).

The gradient Richardson number closely followed the variation in Ri_f between Ozmidov-limited and boundary-influenced samples, with median Ri_g of 0.25 and 0.16, respectively. This correlation suggests that the upper bound of mixing efficiency is set by the available gradients of density and velocity. The minor attenuation of Ri_f relative to Ri_g for the Ozmidov-limited samples is consistent with the hypothesis of Trowbridge (1992) that as Ri_g approaches 0.25 internal waves may play a role in transporting momentum. The decrease in mixing efficiency near the bed is also consistent with the findings of

Trowbridge (1992), which concluded that near a stressed boundary Ri_g and Ri_f are approximately equal and decrease as distance to the boundary decreases. The wall layer is characterized by mixing dominated by boundary-generated turbulence, with minimal stratification effects. In terms of the TKE equation, the stressed boundary is a source of TKE and over time exhausts the near-boundary supply of buoyancy. This leads to a decline in both stratification and buoyancy flux, captured by decreasing Ri_g and Ri_f , respectively. Furthermore, the constant of proportionality between Ri_g and Ri_f can be interpreted as a turbulent Prandtl number (Stacey et al. 1999):

$$Ri_f \equiv \frac{B}{P} \approx \frac{-g K_\rho \frac{\partial \rho}{\rho \partial z}}{\nu_T \left(\frac{\partial u}{\partial z} \right)^2} = Pr_T^{-1} Ri_g, \quad (11)$$

where K_ρ is the turbulent diffusivity for density, ν_T is the turbulent eddy viscosity, and Pr_T is the turbulent Prandtl number. The present data are insufficient to draw conclusions about the precise value or functional form of Pr_T . However, the inferred values of $Pr_T = 1.14$ (Ozmidov-limited conditions) and 1.07 (boundary-influenced conditions) are consistent with the range of commonly reported values of 0.7–1.3 (Munk and Anderson 1948; Garrett et al. 1993; Schumann and Gerz 1995; Warner et al. 2005). Overall, the implication is that the gradient Richardson number is effectively an upper bound on the flux Richardson number.

The Ozmidov-limited samples span a wide range of Re_b , with the central 70% of the data having Re_b between 800 and 6500, with minimal variation in Ri_f over this range. Even without accounting for the effect of uncorrelated variation in ε , the mean Ozmidov-limited efficiency at $Re_b = 10^4$ was 0.20. In contrast, the results of Shih et al. (2005) and Barry et al. (2001) indicate a strong negative dependence of Ri_f on Re_b at high values of Re_b . In fact, their hypothesized relationship would predict efficiencies an order of magnitude lower at $Re_b = 10^4$. In the present data, most of the decrease in efficiency is consistent with the influence of nearby boundaries, as shown in Fig. 10. We hypothesize that the apparent decrease in Re_b found in these earlier studies may arise from similar boundary effects, whether through geometric limitations on the largest scales of turbulence or modification of density and velocity gradients in the vicinity of boundaries. Interpretation of these contrasting relationships may benefit from the Re_T – Fr_T diagram of Ivey and Imberger (1991). The three relevant length scales are the stratification length scale, here taken to be L_O , the eddy overturn scale L_C , and the Kolmogorov

scale η . These length scales can be combined to yield three nondimensional ratios:

$$Re_T = \left(\frac{L_C}{\eta} \right)^{4/3}, \quad (12)$$

$$Fr_T = \left(\frac{L_O}{L_C} \right)^{2/3}, \quad \text{and} \quad (13)$$

$$Re_b = \left(\frac{L_O}{\eta} \right)^{2/3} = Fr_T^2 Re_T. \quad (14)$$

They found that Ri_f was primarily a function of Fr_T , with a maximal value of 0.2 at $Fr_T \approx 1$. To the extent that one can assume that $Fr_T \geq 1$ and $Ri_f \approx f(Fr_T)$, it is clear that a relationship between Ri_f and Re_b would be ambiguous. While a thorough analysis of the observed turbulence overturn scales is beyond the scope of this manuscript, the notion of Ozmidov-limited turbulence is essentially a statement that $Fr_T = 1$, implying that for these samples $Re_T \sim Re_b$. Boundary-limited samples would correspond to $Fr_T > 1$, consistent with $Ri_f < 0.2$ and eddy overturn scales smaller than the stratification scale.

A potential mechanism for the role of boundaries in attenuating mixing efficiency is the simple kinematic constraint on turbulent length scales. Turbulent eddies give up their kinetic energy to potential energy as they displace a parcel away from its stable elevation. When the vertical excursion of this displacement is limited by a boundary, the conversion of kinetic energy to potential energy is also limited, which limits the efficiency of the mixing. Differences between the overturning scale and the Ozmidov scale, for example, the observation in Barry et al. (2001) that $L_E \ll L_O$ when $Re_b > 100$, suggests that turbulent length scales may be limited by some factor other than stratification, leading to less efficient mixing.

Variation in apparent mixing efficiency is also driven by factors beyond the influence of boundaries. While the role of boundaries is a dominant control on efficiency, Ozmidov-limited samples exhibited two additional, though smaller, modes of variation visible in Fig. 10. For $Re_b > 600$, Ri_f had a slight negative correlation with Re_b . An analysis of synthetic data with a prescribed efficiency and modeled variance reproduced a similar, minor trend in efficiency, suggesting that the trend is nonphysical and instead attributable to the nonlinear effects of variance in measured dissipation rates. This synthetic analysis also highlights the potential pitfalls in comparing parameters that have hidden correlations, particularly those involving highly variable, high-order parameters like ε . A second minor trend is visible in Fig. 10, where efficiency appears to decrease at low

values of Re_b . Such a rolloff would be consistent with the flow approaching nonturbulent conditions, though the data density is insufficient to strongly support the trend and the corresponding range of Re_b is much greater than the turbulence threshold of 15 from [Saggio and Imberger \(2001\)](#).

Estimates of buoyancy flux were sensitive to the background density gradient N . Values of Ri_f were compared using N from each of four different methods, with three of the methods producing similar results and a fourth method based on relatively short vertical averaging windows producing greater estimates of Ri_f . Of the four methods, three relied on averages extracted from the CTD profiles and varied only in how the vertical averaging window was chosen, while the last method N_b used finite differences between the fixed CTDs on the MAST. The resulting efficiencies were statistically indistinguishable between N_{ref} , $N_{1.0}$, and N_b . The smaller vertical averaging scale of 0.1 m used in $N_{0.1}$ yielded values of Ri_f that were significantly greater than from other methods. This is consistent with $N_{0.1}$ having more variance independent of the turbulent state, which added positive bias to Ri_f by virtue of introducing noise into the denominator of B . Of the other three methods, we have chosen N_{ref} because it is independent of any ad hoc choices for the vertical scale. While it is encouraging that two other methods produced similar results, it would be difficult to know a priori that these methods and length scales would be appropriate in a flow with significantly different vertical structure.

The methods used to estimate mixing efficiency were based on assumptions of approximate equilibrium and isotropy. The large observed Re_b indicated that isotropy can be assumed in the inertial subrange ([Gargett et al. 1984](#); [Scully et al. 2011](#)). The assumption of equilibrium allows the omission of time-varying and TKE transport terms in the derivation of (1). The continuous forcing by the tidal flow, persistence of mixing layers across transects, and large spatial extent of mixing layers (cf. [Fig. 7](#)) supported the assumption of quasi-steady-state conditions. Transport of TKE at the scale of turbulent braids and billows was effectively averaged out in the analysis and was not a likely source of bias in Ri_f estimates. Vertical transport of TKE at the scale of the mixing layer, however, leads to a potentially significant departure from a balance between P and $\varepsilon + B$ (as in [Scully et al. 2011](#)) and would not be averaged out in our analysis. If efficiency were calculated according to the definition $Ri_f \equiv B/P$, a divergence or convergence in TKE transport would clearly bias the results. The effect of TKE transport on apparent mixing efficiency, as calculated by $Ri_f \approx B/(B + E)$, is unknown. A divergence in TKE flux decreases the energy available for both

viscous dissipation and buoyancy flux, and assuming that this decrease does not favor one sink over the other, we do not expect that it would introduce a major bias into estimates of overall efficiency.

Recent DNS experiments evaluating mixing efficiency in shear flows ([Mashayek et al. 2013](#)) have found a mixing efficiency reaching a nominal value of $1/3$, but with significant variability as a shear instability ages. A similar time-varying efficiency was investigated in [Smyth et al. \(2001\)](#), though that study arrived at a lower nominal efficiency. Efficiencies of $1/3$ are distinctly greater than the majority of field estimates, including the present study. An advantage of DNS approaches is that potential and kinetic energy distributions are explicitly resolved and assumptions of isotropy or equilibrium are not required. To that end, [Mashayek et al. \(2013\)](#) argued that preturbulent, two-dimensional stirring motions, driven by Kelvin–Helmholtz instability, enhance the mixing efficiency. The field observations presented here may have less contribution of preturbulent stirring due to the more persistent turbulent conditions in the continually forced, stratified shear layer. Future DNS simulations with conditions more consistent with these observations will determine whether these differences in efficiency are due to limitations in the field estimates or to actual differences in efficiency between the continually forced and isolated instabilities.

5. Summary and conclusions

Observations of velocity and salinity were collected in two frontal regions of a tidal salt wedge estuary throughout the ebb tide. During the early to midebb, the lower layer was nearly stationary, and both acoustic backscatter and spectral analysis showed intense mixing at the midwater column. Acoustic backscatter across the pycnocline frequently showed distinct shear instabilities with highly turbulent braids, and inertial subrange methods estimated TKE dissipation rates as great as $10^{-3} \text{ m}^2 \text{ s}^{-3}$. Under these conditions, when the bottom boundary was not dynamically significant, Ri_g was maintained near the critical value of $1/4$ for much of the transect. As the ebb progressed and the lower layer was mixed away, the flow transitioned to a stratified bottom boundary layer, with lower Ri_g and ε and less structure in the acoustic backscatter.

High-frequency velocity and conductivity data were collected using ship-mounted instruments, and TKE dissipation rates, buoyancy flux, and mixing efficiency were then estimated with inertial subrange methods. Calculated mixing efficiency was sensitive to the method used for quantifying stratification. A method based on the Ellison scale, developed to be consistent with the

physics of the mixing processes, yielded results similar to two other methods but without the need for an ad hoc choice of vertical length scale.

Turbulence data were divided into two categories, Ozmidov limited and boundary influenced, based on L_O and the distance from the bed. The mean mixing efficiency for all Ozmidov-limited samples was $Ri_f = 0.23 \pm 0.01$ ($\Gamma = 0.30 \pm 0.02$), with a corresponding median $Ri_g = 0.25$. In contrast, the boundary-limited samples (a significantly smaller subset) had a mean $Ri_f = 0.17 \pm 0.02$ ($\Gamma = 0.20 \pm 0.03$) and median $Ri_g = 0.16$. Among the Ozmidov-limited samples, Ri_f was not found to have a significant correlation with increasing Re_b . Given the high values of Re and Re_b , $Ri_f = 0.23$ may approximate an asymptotic maximum for efficiency in continuously forced mixing, hypothesized to be slightly less than the critical $Ri_g = 0.25$ (Trowbridge 1992). These estimates also support the theoretical upper bound on efficiency given by the gradient Richardson number with a turbulent Prandtl number $Pr_T \approx 1$.

Acknowledgments. Holleman was supported by the Devonshire Scholars program. The field study and the coauthors' contributions were supported by NSF Grant OCE 0926427.

REFERENCES

- Barry, M. E., G. N. Ivey, K. B. Winters, and J. Imberger, 2001: Measurements of diapycnal diffusivities in stratified fluids. *J. Fluid Mech.*, **442**, 267–291, doi:10.1017/S0022112001005080.
- Dillon, T. M., 1982: Vertical overturns: a comparison of Thorpe and Ozmidov length scales. *J. Geophys. Res.*, **87**, 9601–9613, doi:10.1029/JC087iC12p09601.
- Ellison, T. H., 1957: Turbulent transport of heat and momentum from an infinite rough plane. *J. Fluid Mech.*, **2**, 456–466, doi:10.1017/S0022112057000269.
- Gargett, A. E., T. R. Osborn, and P. W. Nasmyth, 1984: Local isotropy and the decay of turbulence in a stratified fluid. *J. Fluid Mech.*, **144**, 231–280, doi:10.1017/S0022112084001592.
- Garrett, C., P. MacCready, and P. Rhines, 1993: Boundary mixing and arrested Ekman layers: Rotating stratified flow near a sloping boundary. *Annu. Rev. Fluid Mech.*, **25**, 291–323, doi:10.1146/annurev.fl.25.010193.001451.
- Geyer, W. R., M. E. Scully, and D. K. Ralston, 2008: Quantifying vertical mixing in estuaries. *Environ. Fluid Mech.*, **8**, 495–509, doi:10.1007/s10652-008-9107-2.
- Gibson, C. H., 1986: Internal waves, fossil turbulence, and composite ocean microstructure spectra. *J. Fluid Mech.*, **168**, 89–117, doi:10.1017/S0022112086000307.
- Gregg, M. C., 1999: Uncertainties and limitations in measuring ϵ and χ_t . *J. Atmos. Oceanic Technol.*, **16**, 1483–1490, doi:10.1175/1520-0426(1999)016<1483:UALIMA>2.0.CO;2.
- Inoue, R., and W. D. Smyth, 2009: Efficiency of mixing forced by unsteady shear flow. *J. Phys. Oceanogr.*, **39**, 1150–1166, doi:10.1175/2008JPO3927.1.
- Ivey, G. N., and J. Imberger, 1991: On the nature of turbulence in a stratified fluid. Part I: The energetics of mixing. *J. Phys. Oceanogr.*, **21**, 650–658, doi:10.1175/1520-0485(1991)021<0650:OTNOTI>2.0.CO;2.
- Kaimal, J. C., Y. Izumi, J. C. Wyngaard, and R. Cote, 1972: Spectral characteristics of surface-layer turbulence. *Quart. J. Roy. Meteor. Soc.*, **98**, 563–589, doi:10.1002/qj.49709841707.
- Kay, D. J., and D. A. Jay, 2003: Interfacial mixing in a highly stratified estuary. 1. Characteristics of mixing. *J. Geophys. Res.*, **108**, 3072, doi:10.1029/2000JC000252.
- Lavery, A. C., W. R. Geyer, and M. E. Scully, 2013: Broadband acoustic quantification of stratified turbulence. *J. Acoust. Soc. Amer.*, **134**, 40–54, doi:10.1121/1.4807780.
- MacDonald, D. G., and W. R. Geyer, 2004: Turbulent energy production and entrainment at a highly stratified estuarine front. *J. Geophys. Res.*, **109**, C05004, doi:10.1029/2003JC002094.
- Macoun, P., and R. Lueck, 2004: Modelling the spatial response of the airfoil shear probe using different sized probes. *J. Atmos. Oceanic Technol.*, **21**, 284–297, doi:10.1175/1520-0426(2004)021<0284:MTSROT>2.0.CO;2.
- Mashayek, A., and W. R. Peltier, 2013: Shear-induced mixing in geophysical flows: Does the route to turbulence matter to its efficiency? *J. Fluid Mech.*, **725**, 216–261, doi:10.1017/jfm.2013.176.
- , C. P. Caulfield, and W. R. Peltier, 2013: Time-dependent, non-monotonic mixing in stratified turbulent shear flows: implications for oceanographic estimates of buoyancy flux. *J. Fluid Mech.*, **736**, 570–593, doi:10.1017/jfm.2013.551.
- Moum, J. N., 1996: Efficiency of mixing the main thermocline. *J. Geophys. Res.*, **101**, 12 057–12 069, doi:10.1029/96JC00508.
- , D. M. Farmer, W. D. Smyth, L. Armi, and S. Vagle, 2003: Structure and generation of turbulence at interfaces strained by internal solitary waves propagating shoreward over the continental shelf. *J. Phys. Oceanogr.*, **33**, 2093–2112, doi:10.1175/1520-0485(2003)033<2093:SAGOTA>2.0.CO;2.
- Müller, P., and C. Garrett, 2002: From stirring to mixing in a stratified ocean. *Oceanography*, **15**, 12–19, doi:10.5670/oceanog.2002.10.
- Munk, W. H., and E. R. Anderson, 1948: Notes on the theory of the thermocline. *J. Mar. Res.*, **3**, 276–295.
- Nash, J. D., and J. N. Moum, 2002: Microstructure estimates of turbulent salinity flux and the dissipation spectrum of salinity. *J. Phys. Oceanogr.*, **32**, 2312–2333, doi:10.1175/1520-0485(2002)032<2312:MEOTSF>2.0.CO;2.
- Oakey, N. S., 1982: Determination of the rate of dissipation of turbulent energy from simultaneous temperature and velocity shear microstructure measurements. *J. Phys. Oceanogr.*, **12**, 256–271, doi:10.1175/1520-0485(1982)012<0256:DOTROD>2.0.CO;2.
- Osborn, T., 1980: Estimates of the local rate of vertical diffusion from dissipation measurements. *J. Phys. Oceanogr.*, **10**, 83–89, doi:10.1175/1520-0485(1980)010<0083:EOTLRO>2.0.CO;2.
- , and C. Cox, 1972: Oceanic fine structure. *Geophys. Fluid Dyn.*, **3**, 321–345, doi:10.1080/03091927208236085.
- Peters, H., 1997: Observations of stratified turbulent mixing in an estuary: Neap-to-spring variations during high river flow. *Estuarine Coastal Shelf Sci.*, **45**, 69–88, doi:10.1006/ecss.1996.0180.
- Ruddick, B., D. Walsh, and N. Oakey, 1997: Variations in apparent mixing efficiency in the North Atlantic Central Water. *J. Phys. Oceanogr.*, **27**, 2589–2605, doi:10.1175/1520-0485(1997)027<2589:VIAMEI>2.0.CO;2.
- Saggio, A., and J. Imberger, 2001: Mixing and turbulent fluxes in the metalimnion of a stratified lake. *Limnol. Oceanogr.*, **46**, 392–409, doi:10.4319/lo.2001.46.2.0392.

- Schumann, U., and T. Gerz, 1995: Turbulent mixing in stably stratified shear flows. *J. Appl. Meteor.*, **34**, 33–48, doi:[10.1175/1520-0450-34.1.33](https://doi.org/10.1175/1520-0450-34.1.33).
- Scully, M. E., W. R. Geyer, and J. H. Trowbridge, 2011: The influence of stratification and nonlocal turbulent production on estuarine turbulence: An assessment of turbulence closure with field observations. *J. Phys. Oceanogr.*, **41**, 166–185, doi:[10.1175/2010JPO4470.1](https://doi.org/10.1175/2010JPO4470.1).
- Seim, H. E., and M. C. Gregg, 1994: Detailed observations of a naturally occurring shear instability. *J. Geophys. Res.*, **99**, 10 049–10 073, doi:[10.1029/94JC00168](https://doi.org/10.1029/94JC00168).
- , and —, 1995: Energetics of a naturally occurring shear instability. *J. Geophys. Res.*, **100**, 4943–4958, doi:[10.1029/94JC03199](https://doi.org/10.1029/94JC03199).
- Shaw, W. J., J. H. Trowbridge, and A. H. Williams III, 2001: Budgets of turbulent kinetic energy and scalar variance in the continental shelf bottom boundary layer. *J. Geophys. Res.*, **106**, 9551–9564, doi:[10.1029/2000JC000240](https://doi.org/10.1029/2000JC000240).
- Shih, L. H., J. Koseff, G. N. Ivey, and J. H. Ferziger, 2005: Parameterization of turbulent fluxes and scales using homogeneous sheared stably stratified turbulence simulations. *J. Fluid Mech.*, **525**, 193–214, doi:[10.1017/S0022112004002587](https://doi.org/10.1017/S0022112004002587).
- Smyth, W. D., J. N. Moum, and D. R. Caldwell, 2001: The efficiency of mixing in turbulent patches: Inferences from direct simulations and microstructure observations. *J. Phys. Oceanogr.*, **31**, 1969–1992, doi:[10.1175/1520-0485\(2001\)031<1969:TEOMIT>2.0.CO;2](https://doi.org/10.1175/1520-0485(2001)031<1969:TEOMIT>2.0.CO;2).
- Stacey, M. T., S. G. Monismith, and J. R. Burau, 1999: Observations of turbulence in a partially stratified estuary. *J. Phys. Oceanogr.*, **29**, 1950–1970, doi:[10.1175/1520-0485\(1999\)029<1950:OOTIAP>2.0.CO;2](https://doi.org/10.1175/1520-0485(1999)029<1950:OOTIAP>2.0.CO;2).
- St. Laurent, L. C., J. M. Toole, and R. W. Schmitt, 2001: Buoyancy forcing by turbulence above rough topography in the abyssal Brazil Basin. *J. Phys. Oceanogr.*, **31**, 3476–3495, doi:[10.1175/1520-0485\(2001\)031<3476:BFBTAR>2.0.CO;2](https://doi.org/10.1175/1520-0485(2001)031<3476:BFBTAR>2.0.CO;2).
- Tennekes, H., and J. Lumley, 1972: *A First Course in Turbulence*. MIT Press, 300 pp.
- Thorpe, S. A., 1977: Turbulence and mixing in a Scottish Loch. *Philos. Trans. Roy. Soc. London*, **A286**, 125–181, doi:[10.1098/rsta.1977.0112](https://doi.org/10.1098/rsta.1977.0112).
- , 2005: *The Turbulent Ocean*. Cambridge University Press, 439 pp.
- Trowbridge, J. H., 1992: A simple description of the deepening and structure of a stably stratified flow driven by a surface stress. *J. Geophys. Res.*, **97**, 15 529–15 543, doi:[10.1029/92JC01512](https://doi.org/10.1029/92JC01512).
- Warner, J. C., C. R. Sherwood, H. G. Arango, and R. P. Signell, 2005: Performance of four turbulence closure models implemented using a generic length scale method. *Ocean Modell.*, **8**, 81–113, doi:[10.1016/j.ocemod.2003.12.003](https://doi.org/10.1016/j.ocemod.2003.12.003).